Solar Energy 155 (2017) 637–646

Contents lists available at ScienceDirect

Solar Energy

journal homepage: www.elsevier.com/locate/solener

Optical losses of photovoltaic cells due to aerosol deposition: Role of particle refractive index and size

Patricio Piedra *, Hans Moosmüller

Laboratory for Aerosol Science, Spectroscopy, and Optics, Desert Research Institute, Nevada System of Higher Education, 2215 Raggio Parkway, Reno, NV 89512, USA

ARTICLE INFO

Article history:
Received 10 January 2017
Received in revised form 7 June 2017
Accepted 13 June 2017

Keywords:
Photovoltaic
Optical degradation
Deposition
Soiling

ABSTRACT

Field experiments have revealed that deposition of dust particles plays a significant role in optical degradation of photovoltaic (PV) cell performance. Such experiments have been performed as a function of tilt angle of the cells, exposure time, and other environmental factors. However, very little is known about cell degradation as function of intensive particle parameters such as size and complex refractive index. This paper shows that, for normally incident solar radiation, deposited aerosols degrade PV cell performance due to particle absorption and due to scattering into the backward hemisphere. The fraction power lost (*FL*), together with the optical depth of the deposited particles, determines the fraction of power lost from the incident light beam. We have performed scattering calculations simulating the interaction of light with particles on substrates that analyzed *FL* as function of particle size and particle complex refractive index. We have found that for small particles and a relatively large imaginary part of their refractive index, absorption losses dominate while for large particles and a relatively small imaginary part of the refractive index, backscattering losses dominate. Per optical depth, fine particles result in higher optical losses than coarse ones due to their larger absorption and hemispheric backscattering. Overall, our work quantifies optical losses caused by deposited aerosols toward the goals of estimating PV cell performance for energy forecasting, informing PV cell designers about potential efficiency losses caused by particle deposition, and optimizing cleaning schedules.

1. Introduction

The need for energy forecasting has become a pressing issue in supporting smarter grids that can predict fluctuations, reduce or eliminate outages, and charge flexible prices. In recent years, significant efforts have been dedicated to create systems that allow for solar power forecasting (Pelland et al., 2013). One of such forecasting factors is the power loss due to aerosol deposition such as dust, pollen, carbonaceous particles, etc.

From the fundamental physics perspective, the goal of PV energy harvesting is simple: to maximize the conversion of solar electromagnetic (EM) energy into electrical energy. Aerosol deposition on PV cells adds complexity to this goal. Aerosol particles deposited on PV cells absorb and backscatter part of the incident optical power and thereby reduce the optical power transmitted to the PV cell itself. This problem is significant since a large number of PV cells are located in sunny, semi-arid regions, where they can be subject to frequent deposition of mineral dust and other particles (e.g., soot in polluted areas). Field studies of PV cell degradation by dust deposition reveal that deposited aerosols significantly reduce the efficiency of PV cells, with studies reporting up to 85% losses (Sulaiman et al., 2014).

Many experiments on this subject report power transmission losses as function of time of exposure of the PV cell to its environment (Mani and Pillai, 2010; Maghami et al., 2016). However, there exists little work on understanding transmission losses that depend on the intrinsic optical characteristics of the deposited particles. Here, we study the transmittance properties of aerosols deposited on PV cells. We deviate from approaches that consider solely light extinction (Al-Hasan, 1998). Instead, we distinguish hemispherical forward scattering from hemispherical backward scattering, include absorption, and also consider the optical interaction between the PV cell surface and the deposited particles.

2. Power losses due to particle deposition on PV cells

In order to develop the following theoretical framework, let us consider a very simple scenario of a PV cell with low particle loading (e.g., particles have not deposited onto other particles). Furthermore, let us assume that particles have deposited sparsely and homogeneously (i.e., particles do not form clusters), and light

* Corresponding author.
E-mail address: patriciopiedra@gmail.com (P. Piedra).

http://dx.doi.org/10.1016/j.solener.2017.06.047
0038-092X/

is normally incident. A summary of simplifying assumptions of this study and future work needed is shown in Table 1.

The power incident at normal incidence onto a clean PV cell and converted to electricity is P_0. If the PV cell is dirty, the power of the direct beam is reduced to P by particle scattering and absorption according to Beer-Lambert's law (e.g., Moosmüller et al., 2009)

$$P = P_0 e^{-\tau_{ext}}, \tag{1}$$

where τ_{ext} is the extinction optical depth caused by aerosols deposited on the substrate. The extinction optical depth is a measure of the amount of light that is removed from the incident beam due to scattering and absorption. The conventional term "optical depth" is misleading as it implies units of length, while τ_{ext} is unitless. For $\tau_{ext} \ll 1$, it can be written as the sum of scattering and absorption optical depths as

$$\tau_{ext} = \tau_{sca} + \tau_{abs}. \tag{2}$$

Here, we consider only the simplest case of light at normal incidence where we further distinguish between optical depth from scattering into the forward hemisphere τ_{fs} and from scattering into the backward hemisphere τ_{bs} by writing $\tau_{sca} = \tau_{fs} + \tau_{bs}$, yielding the identity

$$\tau_{ext} - \tau_{fs} = \tau_{bs} + \tau_{abs}. \tag{3}$$

Dividing the identity of Eq. (3) by τ_{ext}, we obtain

$$1 - \frac{\tau_{fs}}{\tau_{ext}} = \frac{\tau_{bs} + \tau_{abs}}{\tau_{ext}}. \tag{4}$$

Let us define the power fraction lost FL as the fraction of extinction optical depth that is due to absorption and scattering into the backward hemisphere direction as

$$FL \equiv \frac{\tau_{bs} + \tau_{abs}}{\tau_{ext}} = \frac{\sigma_{bs} + \sigma_{abs}}{\sigma_{ext}}, \tag{5}$$

where σ represents optical cross section instead of optical depth τ so that σ_{abs} is the absorption cross section, σ_{ext} is the extinction cross section, and σ_{bs} is the hemispherical backward scattering cross section. For the PV cell surface being normal to the direction of the incident solar radiation, the power from extinction due to hemispherical forward scattering still reaches the semiconductor material and produces electrical power, while the extinction due to absorption heats the absorbing particles and the extinction due to hemispherical backward scattering is lost from the system. Therefore, the optical power P_{sc} reaching the semiconductor material after interacting with deposited particles can be written as

$$P_{sc} = P_0 e^{-(\tau_{abs} + \tau_{bs})} = P_0 e^{-\tau_{ext} FL}. \tag{6}$$

For $\tau_{ext} FL \ll 1$, we can approximate Eq. (6) using the identity $e^{\beta} \approx 1 + \beta$ for $\beta \ll 1$ as

$$P_{sc} \approx P_0 (1 - \tau_{ext} FL). \tag{7}$$

For the simplest case of N identical particles with extinction cross-sections σ_{ext} deposited onto a surface area A, the deposited particle layer has an optical depth τ_{ext} with

$$\tau_{ext} = \frac{N}{A} \sigma_{ext}. \tag{8}$$

and the fraction lost is given by Eq. (5). However, in reality aerosol particles have a size distribution $n(x) = \frac{\delta N}{\delta x}$, where $\int_{x_1}^{x_2} n(x) dx = N$; for spherical particles, the size parameter x is the ratio of the particle circumference πD (with D being the particle diameter) to the EM wave's wavelength λ with x defined as

$$x = \pi \frac{D}{\lambda}. \tag{9}$$

If the sample is polydisperse with size parameters x between x_1 and x_2, Eq. (8) must be replaced by

$$\tau_{ext} = \frac{1}{A} \int_{x_1}^{x_2} n(x) \sigma_{ext}(x) dx, \tag{10}$$

while the numerator of Eq. (5) is given by

$$\tau_{bs} + \tau_{abs} = \frac{1}{A} \int_{x_1}^{x_2} n(x) [\sigma_{bs}(x) + \sigma_{abs}(x)] dx. \tag{11}$$

Thus, for polydisperse particles, Eq. (5) becomes

$$FL = \frac{\int_{x_1}^{x_2} n(x) [\sigma_{bs}(x) + \sigma_{abs}(x)] dx}{\int_{x_1}^{x_2} n(x) \sigma_{ext}(x) dx}. \tag{12}$$

Table 1
Overview of assumptions of this study and future work needed.

	This paper	Future work needed
Incoming Radiation	– direction normal to PV cell – only direct radiation	– as function of incident angle – consider diffuse/direct radiation – consider polarization effects
Particles	– homogeneous spheres – fixed real Ref. index, varying imaginary Ref. index – low optical depth – homogeneous spatial distribution	– other shapes – inhomogeneous particles – as function of real refractive index – high/any optical depth – inhomogeneous spatial distribution
Surface	– calculates surface interaction, but only for thick surface with Ref. index $n = 1.5$	– consider thin layered surfaces (e.g., anti-reflective coatings) – varying complex Ref. index
Experimental Work	– none	– needed

2.1. Intensive vs. extensive optical parameters

A subtle but important distinction arises from describing light attenuation in the manner described in Section 2. Eq. (1) has been modified to Eq. (6) through the definition of FL in Eq. (5). This modification allow us to describe power transmission into the PV cell semiconductor as

$$P_{sc} = P_0 e^{-\tau_{eff}}, \tag{13}$$

where the effective (photovoltaic) optical depth τ_{eff} is

$$\tau_{eff} = \frac{N}{A} \sigma_{ext} FL = \rho_N \sigma_{ext} FL. \tag{14}$$

The quantity $\rho_N \equiv \frac{N}{A}$ is the number density of particles per unit area on the PV cell with units of m^{-2}. Alternatively, we can use the mass extinction cross section k_{ext} (i.e., the extinction cross section per unit mass) with units of m^2/kg to describe τ_{eff} as

$$\tau_{eff} = \rho_M k_{ext} FL, \tag{15}$$

where ρ_M is the sample mass density per unit area with units of kg/m^2. τ_{eff} is proportional to the particle number density ρ_N or the sample mass density ρ_M. These quantities are extensive in the sense that they proportional to the amount of particles deposited. The quantities $\sigma_{ext} FL$ and $k_{ext} FL$ are intensive; they are dependent on the optical properties, but not on the quantity of the deposited particles.

The mass extinction cross section k_{ext} is related to the extinction cross section σ_{ext} as

$$k_{ext} = \frac{\sigma_{ext}}{M} = \frac{Q_{ext}\sigma_{geo}}{M}, \tag{16}$$

where Q_{ext} is the extinction efficiency (i.e., the extinction cross section divided by the geometric cross section), σ_{geo} is the particle geometric cross section and M is the particle mass. If we assume that all particles are spherical and the sample is mono-disperse, $M = \frac{\pi}{6}\rho D^3$ (where ρ is particle mass density), and also $\sigma_{geo} = \frac{\pi}{4}D^2$. Expressing D in terms of size parameter x yields

$$k_{ext} = \frac{3\pi}{2\rho\lambda x}Q_{ext}. \tag{17}$$

Hence, Eq. (15) can be written as

$$\tau_{eff} = \frac{3\pi\rho_M}{2\rho\lambda x}[Q_{ext}FL]. \tag{18}$$

The fraction ρ_M/ρ has dimension of length and is a measure of the average thickness of the particle layer. The intensive particle optical properties determine $[Q_{ext}FL]$ in Eq. (18), and quantify the hemispherical backward scattering and absorption efficiency, or *BSAE* for short

$$BSAE \equiv Q_{ext}FL. \tag{19}$$

We explore the behavior of *FL* and *BSAE* in Section 4.

Eq. (18), which yields $Q_{ext}FL$ as an important factor determining τ_{eff}, is simple and arises from our assumptions that all particles are spherical and that all particles are of the same size. While this is a very simplistic model, it allows us to investigate the optical effects of particles on PV cells with respect to their size and complex refractive index. In a more general approach, abandoning mono-disperse assumptions, the mass extinction cross section must be integrated over all sizes x with $x_1 \leqslant x \leqslant x_2$, yielding

$$k_{ext} = \frac{\int_{x_1}^{x_2}\sigma_{ext}(x)n(x)dx}{\rho\int_{x_1}^{x_2}v(x)n(x)dx}, \tag{20}$$

where $v(x)$ is the particle volume with size parameter x and $n(x)dx$ is the number of particles with size parameter x. Substituting $\sigma_{ext}(x) = Q_{ext}(x)\frac{\pi}{4}D^2$ and $v(x) = \frac{\pi}{6}D^3$, and replacing $D = \frac{x\lambda}{\pi}$, yields

$$k_{ext} = \frac{3\pi}{2\rho\lambda}\frac{\int_{x_1}^{x_2}Q_{ext}(x)x^2n(x)dx}{\int_{x_1}^{x_2}x^3n(x)dx}. \tag{21}$$

Hence,

$$\tau_{eff} = \frac{3\pi\rho_M}{2\rho\lambda}\left[\frac{\int_{x_1}^{x_2}Q_{ext}(x)x^2n(x)dx}{\int_{x_1}^{x_2}x^3n(x)dx}FL\right] \tag{22}$$

While Eq. (22) is more complex than (18), it contains the same physics, just integrating it over a particle size distribution.

3. Calculation of particle optical properties

In this section, we briefly describe two approaches to calculating particle optical properties. The first one is the well-known Mie theory (Mie, 1908) and the second one is the discrete dipole approximation (DDA) method (Draine and Flatau, 1994). Mie theory is widely used for calculating optical properties of homogeneous, spherical particles in a homogeneous medium, while DDA can be used for particles with more complex morphology (including irregular shapes) and to calculate electromagnetic (EM) scattering of particles on surfaces. An alternative and more efficient method to calculate EM scattering of spheres or spheroids with substrate interaction is the T-matrix method (Videen, 1995; Mackowski, 2008), however, it is not used here. In DDA and Mie theory, it is assumed that an EM plane wave is scattered by a particle, and the incident wave is represented by

$$\boldsymbol{E}_0 = \begin{bmatrix} E_{0r}e^{i\phi_l} \\ E_{0l}e^{i\phi_r} \end{bmatrix} e^{i(\boldsymbol{k}\cdot\boldsymbol{r}-\omega t)}, \tag{23}$$

where the l and r subscripts are used to represent the parallel and perpendicular components (relative to the scattering plane) of the electric field E_0 with corresponding phases ϕ_l and ϕ_r, respectively. The vector $\boldsymbol{k} = \boldsymbol{k_r} + i\boldsymbol{k_i}$ is the complex wave number defined by

$$\boldsymbol{k}\cdot\boldsymbol{k} = \omega^2\epsilon\mu, \tag{24}$$

where ω is the angular frequency, ϵ is the electric permittivity, and μ is the permeability.

The aim of most particle optics calculations is to find a solution to the far-field scattering equation given by

$$\boldsymbol{E}_{sca} = \frac{1}{kr}\begin{bmatrix} s_1 & s_2 \\ s_3 & s_4 \end{bmatrix}\boldsymbol{E}_0, \tag{25}$$

where r is the distance from the center of the particle to the detector, and s_1 through s_4 are the components of the scattering matrix.

3.1. Mie theory

Mie theory (Mie, 1908) has been used widely for determining the optical properties of homogeneous, spherical particles. However, even for non-spherical particles, Mie theory can be used as a first order approximation (Bohren and Huffman, 2008). Mie theory provides a solution to the Helmholtz wave equations. The solution of this system of complex vector differential equations is non-trivial (van de Hulst, 1981), requiring a fair amount of mathematical sophistication. Even when solved, the solution is an infinite series and a computer is generally used to reach a solution within a reasonable time. Nonetheless, Mie theory effectively solves Eq. (25) for homogeneous, spherical particles and yields

$$\boldsymbol{E}_{sca}(x,m,\theta) = \frac{1}{kr}\begin{bmatrix} s_l(x,m,\theta) & 0 \\ 0 & s_r(x,m,\theta) \end{bmatrix}\boldsymbol{E}_0, \tag{26}$$

where $s_2 = s_3 = 0$, due to the spherical symmetry of the particles. The dependency of the scattered electric field $\boldsymbol{E}_{sca}$ on the size parameter x, the index of refraction m, and the scattering angle θ has been explicitly stated to highlight the intensive parameters determining the scattered field. The quantities s_l and s_r are the parallel and perpendicular phase functions, respectively.

3.2. Discrete dipole approximation

The discrete dipole approximation (DDA) is a relatively new method for particle optics calculations that uses numerical computation to estimate a solution for the scattering Eq. (25). DDA was first envisioned by numerical pioneers seeking to take advantage of ever improving computational capabilities. Draine and Flatau (1994) published an open-access FORTRAN code that made DDA widely available. DDA has since been traduced, improved, parallelized, and used in numerous light scattering studies ranging from of optics of blood cells (Maltsev et al., 2011) to analysis of sea-salt aerosols (Chamaillard et al., 2003). DDA is a flexible scattering calculation that discretizes a particle as a collection of point dipoles in space. Considering the interactions of each dipole with one another, DDA inverts an interaction matrix to find a vector solution for the polarizability of each and every point dipole. The final electric field is given by the sum of individual dipole fields (Schmehl, 1994). Here, we used an open access DDA code written in C and developed by Yurkin and Hoekstra (2011) that allows parallel computation on multiprocessor supercomputers.

4. Analysis

We are quantifying the role of index of refraction and particle size on PV cells degradation using the single scattering approximation (i.e., $\tau_{ext} \ll 1$) and assuming a non-reflective semiconductor surface. Light that interacts with a particle on a PV cell can be absorbed or scattered. The sum of these effects is known as extinction. Expressing Eq. (2) in terms of cross sections yields

$$\sigma_{ext} = \sigma_{abs} + \sigma_{sca}, \tag{27}$$

where the subscripts "ext", "abs" and "sca" stand for extinction, absorption, and scattering, respectively. The first term, the absorption cross section σ_{abs}, is a result of the transformation of EM energy into thermal energy. Absorption is associated with the imaginary part of the particle's index of refraction $m = m_r + im_i$, where m_r is the real part and m_i is the imaginary part. For example, the bulk absorption coefficient α is related to m_i as

$$\alpha = \frac{4\pi}{\lambda} m_i(\lambda). \tag{28}$$

Notice that the absorption coefficient depends on the wavelength through the $\frac{1}{\lambda}$ factor and through a possible wavelength dependence of m_i. For many compounds, $m_i(\lambda)$ has been spectroscopically tabulated, for instance by Polyansky (2016). Typical values of m_i in the solar spectrum for aerosols in Earth's atmosphere span many orders of magnitude, ranging from ~ 0 to ~ 1 (Levoni et al., 1997). Through the absorption coefficient, it is possible to define a skin depth δ, that is the distance within the particle necessary to reduce EM incoming power density by $\frac{1}{e^2}$, as

$$\delta = \frac{2}{\alpha} = \frac{\lambda}{2\pi m_i}. \tag{29}$$

In Section 2, we defined the power fraction loss *FL* by Eqs. (5) and (12) and the hemispherical backward scattering and absorption efficiency *BSAE* by Eq. (19). In Section 3, we described the use of scattering theory to calculate the phase functions needed to obtain *FL* and *BSAE*. The hemispherical backward scattering cross section σ_{bs} is obtained by integrating $|\boldsymbol{E}|^2$ over the backward scattering hemisphere of the particle.

In order to better explain our results, we introduce the particle radius to skin depth fraction $m_i x$, where

$$m_i x = \frac{D/2}{\delta} \tag{30}$$

is the ratio of particle radius $D/2$ to the skin depth δ. Thus, two spherical particles with equal $m_i x$ share the same ratio of particle radius to skin depth despite different x or m_i. We shall henceforth refer to $m_i x$ as the radius to skin depth fraction. Wang et al. (2015) have demonstrated that results of EM scattering calculations can be unified if $m_i x$ is used as variable instead of using x and m_i independently.

Seinfeld and Pandis (2012) report that aerosol particle size distributions in the atmosphere strongly depend on the ambient conditions with urban aerosol particle numbers peaking in the range $0.1\ \mu m \lesssim D \lesssim 0.5\ \mu m$; rural continental aerosol number distributions are usually bi-modal with peaks at $\sim 0.02\ \mu m$ and $\sim 0.08\ \mu m$. Desert aerosols number distributions are often tri-modal with number peaks at $D \lesssim 0.01\ \mu m$, $\sim 0.05\ \mu m$, and $\sim 10\ \mu m$. In addition, PV cell conversion efficiency peaks around $\lambda \sim 0.6\ \mu m$, close to the peak of the solar spectrum. The largest particle size at which the number size distribution peaks is for desert aerosol at $D \sim 10\ \mu m$, with a corresponding size parameter x, Eq. (9), of

$$x = \frac{\pi\ 10\ \mu m}{0.6\ \mu m} \sim 50$$

Hence, particles with $x \lesssim 50$ include the majority of aerosols that are deposited on PV cells. Nonetheless, near dust sources, particles as large as $\sim 100\ \mu m$ ($x \sim 524$) can be found. It is noteworthy that airborne particle number size distributions may differ strongly from deposited ones due to deposition mechanisms and accumulation of particles (e.g., Li et al., 2009; Tan et al., 2014). Our study is limited to low, homogeneous deposition loadings (Table 1). DDA-substrate calculations for particles with $x \gtrsim 50$ are computationally very demanding due to the large number of required dipoles. For very large particles, other methods of scattering calculation such as the T-matrix technique (Wriedt and Doicu, 1998) can be used.

4.1. Power fraction lost FL

Fig. 1 shows the power fraction lost *FL* for spherical aerosol particles with size parameter $x = 10$ (corresponding for $\lambda = 0.6\ \mu m$ to a particle with diameter $D \approx 2\ \mu m$) and a refractive index $m = 1.5 + im_i$ as a function of radius to skin depth fraction $m_i x$. The refractive index of the substrate is given by $n = n_r + in_i$, where n_r is the real part, and n_i is the imaginary part. We calculated particle-substrate scattering with DDA using two different refractive indices for the substrate, the first one is $n_r = 1.0$, identical to that of free space (i.e., without substrate), and the second one is $n_r = 1.5$, typical for a glass or fused silica substrate. In both cases, the substrate was assumed to be non-absorbing with an imaginary refractive index $n_i = 0$. As expected, the free-space Mie scattering and DDA particle-substrate results agree when the DDA substrate is removed by assuming its refractive index as $n_r = 1$. Our results (see Fig. 1) indicate that *FL* is nearly constant with $FL \lesssim 0.1$ for $10^{-4} < m_i x < 10^{-2}$. This small and nearly constant power fraction lost is a result of weak absorption for very small m_i, which makes the skin depth much larger than the particle radius. In addition, losses by scattering remain small since most scattering is into the forward hemisphere. For $m_i x$ larger than 10^{-1}, we observe rapid increase in *FL* as function of $m_i x$ due to increased absorption. *FL* peaks at ~ 0.5 for $m_i x \sim 2$ corresponding to the skin depth equal to the particle diameter. This indicates that about half of the interacting power can be lost for particles with $x = 10$ and $m_i \sim 0.2$. When the skin depth is comparable to the diameter of the particle, the absorption efficiency Q_{abs} (i.e., ratio of absorption cross section to geometric cross section) peaks at a maximum value of ~ 1, while

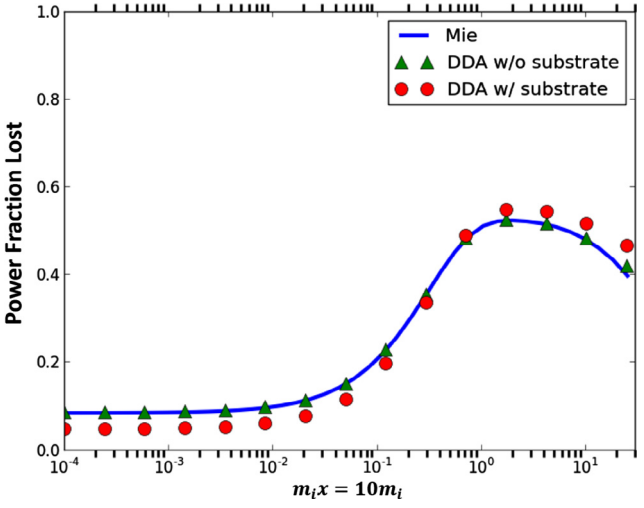

Fig. 1. The power fraction lost *FL* as a function of radius to skin depth fraction $m_i x$ for spherical aerosols with index of refraction $m = 1.5 + im_i$ is shown, where $10^{-4} \leqslant m_i \leqslant 2.5$. The size parameter is $x = 10$ and the corresponding results from Mie calculation are shown as a solid line. The DDA-substrate calculation includes a substrate with refractive index $n_r = 1.5$ or a negligible substrate with $n_r \approx 1$.

the hemispherical backward scattering efficiency remains small. The net effect is that the power fraction lost is dominated by absorption, thus extinguishing about half the interacting power so that $FL \sim \frac{1}{2}$ (see extinction paradox, Bohren and Huffman (2008)). As $m_i x$ becomes even larger, FL starts to decrease. Particles with $m_i \gtrsim 0.2$ start to acquire metallic, more reflective properties, and as the skin depth becomes much smaller than the radius of the particle, penetration of light into the particle is reduced. This results in more scattered light and less absorption, thus we observe FL starting to decline for increasing $m_i x > 2$. A discussion of the effect of the substrate is given later in Section 4.4 "Particle Scattering without and with Substrate."

In Fig. 2, we plot FL as function of $m_i x$ using Mie theory as well as DDA particle-substrate calculations for various size parameters. Similarly to Fig. 1, the particle real refractive index is $m_r = 1.5$, while the substrate real refractive index is $n_r = 1.5$. The plot displays the corresponding curves for size parameters $x = 0.01, 0.1, 0.5, 1, 2, 5, 10$, and 20. If we use $\lambda = 0.6$ μm as our reference wavelength, the corresponding particle diameters are $D \sim 0.002, 0.02, 0.1, 0.2, 0.4, 1, 2$, and 4 μm, respectively. We observe that Mie calculations (no substrate) for small particles in the Rayleigh regime (Moosmüller et al., 2009) such as $x = 0.1$, yield $FL \sim 0.5$ when the radius to skin depth fraction is small ($m_i x \ll 10^{-10}$) because small ($x \ll 1$) particles scatter nearly symmetrically in the forward and backward direction, thereby reducing the transmitted power by about half when absorption is negligible (van de Hulst, 1981 Ch. 6). For these small particles, FL increases rapidly as function of m_i, reaching $FL \sim 1$ at $m_i x \gtrsim 10^{-9}$ for $x = 0.01$ and at $m_i x = 10^{-4}$ for $x = 0.1$. This is because absorption totally dominates over scattering for small ($x < 0.5$) particles in this regime. In addition, as the particle becomes absorbing, the skin depth rapidly decreases to become comparable to the diameter of the particle so that absorption is maximized. For larger particles with $x > 0.5$, the scattering direction is preferentially into the forward hemisphere. Hence, we observe that FL decreases for increasing x. Particles with $0.5 < x < 1$, reach a FL peak at $m_i x \sim 0.5$, that is, when radius to skin depth fraction is approximately a half. This is because losses caused by backward hemispheric scattering are still significant. Larger particles ($x \gtrsim 1$) reach a peak $FL \sim 0.5$ at $m_i x \approx 2$, that is, when the skin depth is approximately the same as the diameter. It is interesting to compare these curves with common measurements of size and imaginary index of refraction of dust and carbonaceous particles. Suspended mineral dust has a complex chemical and mineralogical composition affecting its optical properties (Engelbrecht et al., 2016; Moosmüller et al., 2012). Formenti et al. (2011) report Saharan dust particles size number distributions, the maximum count median diameter for airborne collected samples is ≈ 6.6 μm corresponding for $\lambda = 0.55$ μm to $x \approx 38$. In addition, Ryder et al. (2013) measured Saharan dust's m_i at $\lambda = 0.55$ μm, finding results in the range $10^{-2} \lesssim m_i \lesssim 10^{-3}$ as indicated in Fig. 2. Similarly, black carbon particle refractive indices are reported by Bond and Bergstrom (2006) at $\lambda = 0.55$ μm with results in the range $10^{-1} \lesssim m_i \lesssim 10^{0}$. Black carbon number size distribution over Europe have been studied by Reddington et al. (2013), finding that black carbon number size distributions peak near $D \approx 200$ nm (corresponding to $x \sim 1$ for $\lambda = 0.55$ μm) with standard deviations ranging from $D \sim 50$ nm ($x \sim 0.3$) to $D \sim 400$ nm ($x \sim 2$). These ranges are estimated in Fig. 2 as ovals. The high FL of black carbon explains why experiments of PV cells deposited with carbon particles yield higher losses per optical depth than other types of particles (Darwish et al., 2015).

4.2. Hemispherical Backward Scattering and Absorption Efficiency BSAE

Fig. 3 plots $BSAE = Q_{ext} FL$ as function of $m_i x$ for different particle sizes. For all sizes, $BSAE$ is nearly constant between $10^{-5} \lesssim m_i x \lesssim 10^{-2}$ with the size parameter $x = 5$ having the highest $BSAE \sim 0.4$. $BSAE$s for particles with size $x \geqslant 1$ peak at $m_i x \approx 2$ (where the skin depth is comparable to the radius of the particle). The peak $BSAE$ for these particles decreases as function of size from $BSAE \sim 2.5$ to $BSAE \sim 1$. Fig. 4 gives the same data of Fig. 3 and shows $BSAE$ as function of $m_i x$ for the same size parameters as Figs. 2 and 3, however emphasizing small $BSAE$ through the use of a logarithmic y-axis. Note that $BSAE$ curves for small

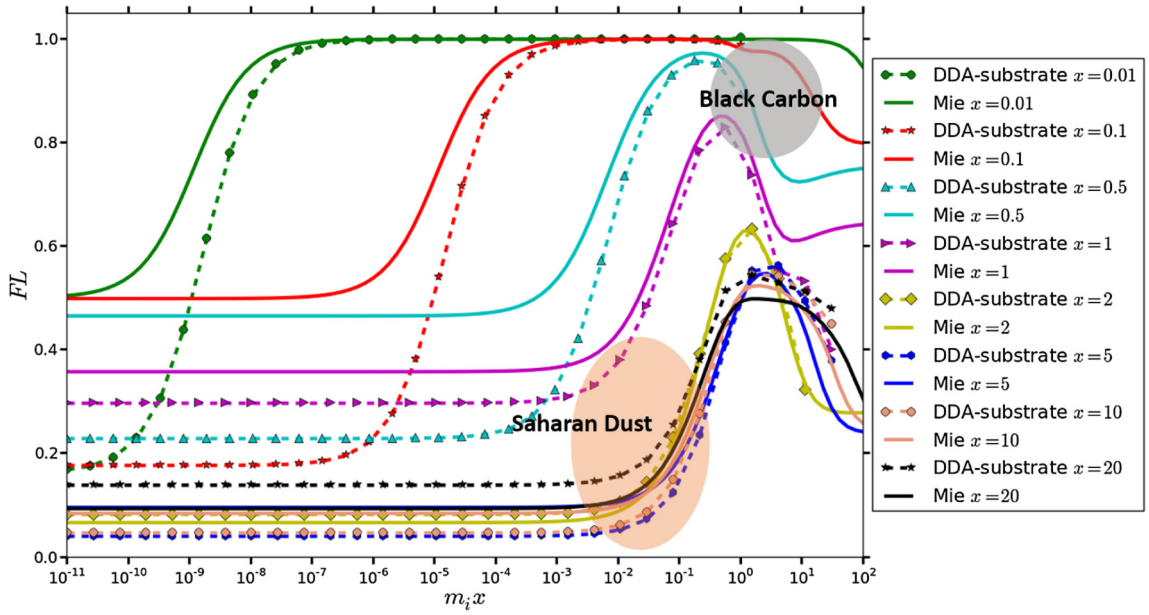

Fig. 2. The power fraction lost FL plotted as a function of $m_i x$ in lin-log scale for spherical aerosols with refractive index $m = 1.5 + im_i$ using both Mie theory and the DDA-substrate method. The refractive index of the substrate is $n = 1.5 + i0$, similar to that of glass and fused silica. Each curve is for one size parameter. Mie calculations are shown as solid colored lines while DDA calculations are shown as markers on dashed lines. The ovals represent an estimation of m_i for Saharan dust and carbonaceous particles

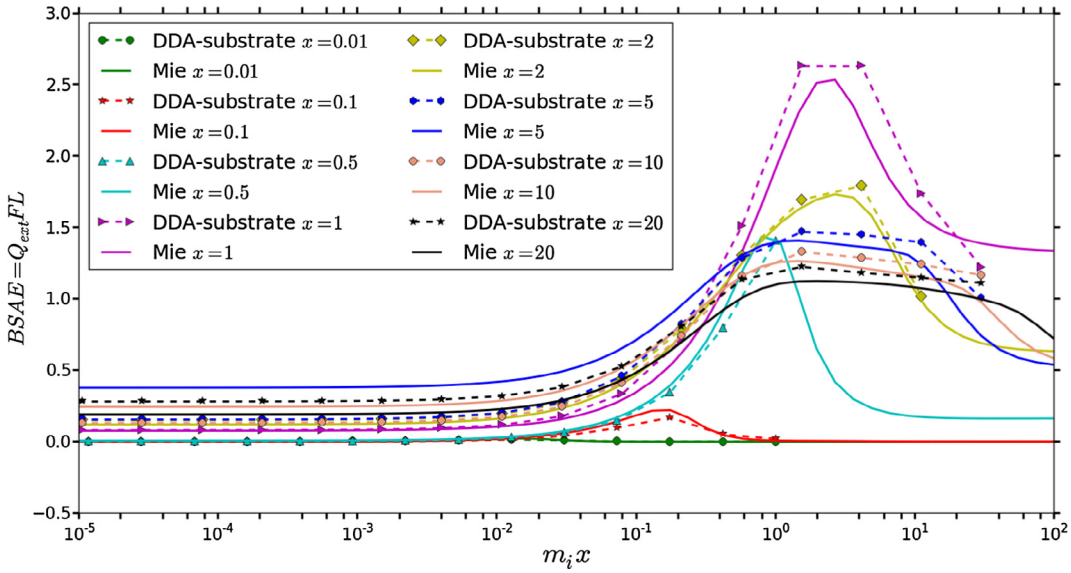

Fig. 3. We show $Q_{ext}FL$ as function of $m_i x$ for spherical aerosols with refractive index $m = 1.5 + im_i$ calculated with Mie theory and DDA-substrate method. The substrate refractive index is $n = 1.5 + i0$, similar to that of glass and fused silica. Mie theory results are displayed as solid colored lines while the corresponding DDA results are shown as markers on dashed lines.

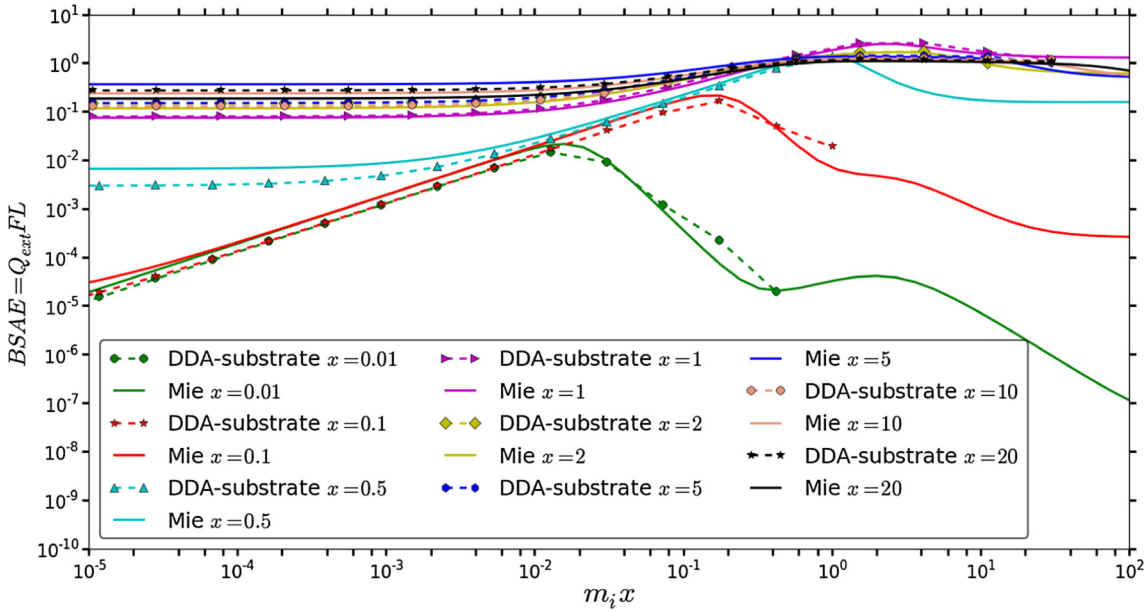

Fig. 4. $BSAE = Q_{ext}FL$ as function of $m_i x$ is shown for spherical particles with refractive index $m = 1.5 + im_i$ in log-log scale by Mie theory and by DDA-substrate method. The refractive index of the substrate is $n = 1.5 + i0$. Curves calculated by Mie theory are shown as a solid lines while DDA-substrate calculations are shown as markers on dashed lines.

particles with size $x \leqslant 1$ are largely different from curves for larger particles with $x > 1$. *BSAE*s for small particles ($x \leqslant 0.5$) have a positive slope as function of $m_i x$, and the starting point of the positive slope shifts substantially right as x increases. For instance, notice the positive slope of the $x = 0.5$ curve which starts at $m_i x \sim 10^{-2}$ and the slope of $x = 1$ which starts at $m_i x \sim 10^{-1}$. In contrast, the positive slopes for larger particles with $x > 1$ start at $m_i x \sim 10^{-1}$ and are not as large as those for smaller particles with $x < 1$. For this reason, *BSAE* of $x = 1$ is actually larger at the peak occurring at $m_i x \approx 2$ than *BSAE*s of particles with $x > 1$. Finally, Fig. 5 shows *BSAE* as function of x (instead of $m_i x$) in log-log space for different m_i. A distinct positive slope is noticed in all curves indicating that *BSAE* generally increases with size, reaching a peak at $x \sim 1$ at which point *BSAE* starts to decrease. The largest *BSAE*s are observed for $m_i = 1$ with a peak of *BSAE* ~ 3. At larger m_i the overall *BSAE* values decrease for all size parameters as can be seen for $m_i = 2$.

4.3. Dominance of absorption or hemispherical backward scattering as loss mechanism

The power fraction lost *FL* is the sum of absorption and hemispherical backward scattering. Either mechanism can dominate *FL* depending on particle size and refractive index. The dominance of either scattering or absorption as mechanism for light extinction is conventionally quantified using the single scattering albedo (*SSA*) defined as

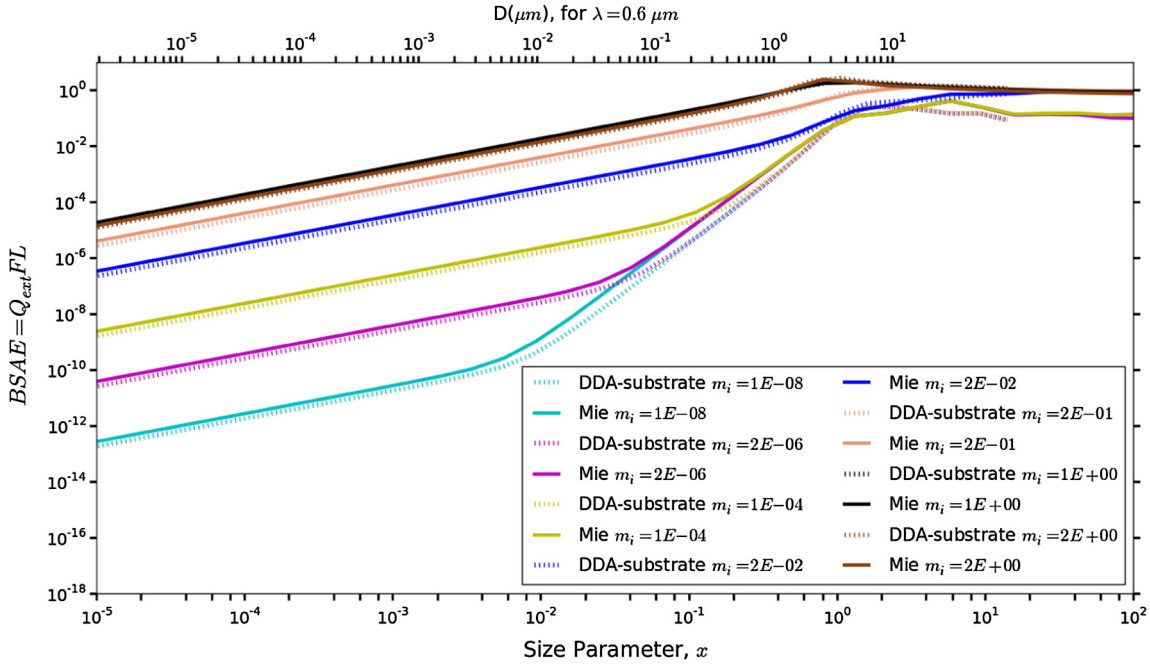

Fig. 5. $BSAE = Q_{ext}FL$ as function of x is shown for m_i in $10^{-8} < m_i < 2$. The upper horizontal axis shows the particle diameter for $\lambda = 0.6$ μm.

$$SSA = \frac{\sigma_{sca}}{\sigma_{abs} + \sigma_{sca}} = \frac{\sigma_{sca}}{\sigma_{ext}}, \tag{31}$$

where *SSA* is the fraction of light extinction that is due to scattering. For our application, we use the co-albedo *COSSA* defined as

$$COSSA = 1 - SSA = \frac{\sigma_{abs}}{\sigma_{ext}}, \tag{32}$$

where *COSSA* is the fraction of light extinction that is due to absorption. The *FL* parameter defined in Eq. (5) can now be written as

$$FL = \frac{\sigma_{bs}}{\sigma_{ext}} + \frac{\sigma_{abs}}{\sigma_{ext}} = BL + COSSA, \tag{33}$$

where *BL* is the fraction of extinction that is due to scattering into the backward hemisphere, defined as

$$BL \equiv \frac{\sigma_{bs}}{\sigma_{ext}} \tag{34}$$

FL and its components *COSSA* and *BL* are plotted in Fig. 6 as a function of the size parameter x for different imaginary parts of the particle's refractive index. COSSA indicates fractional power

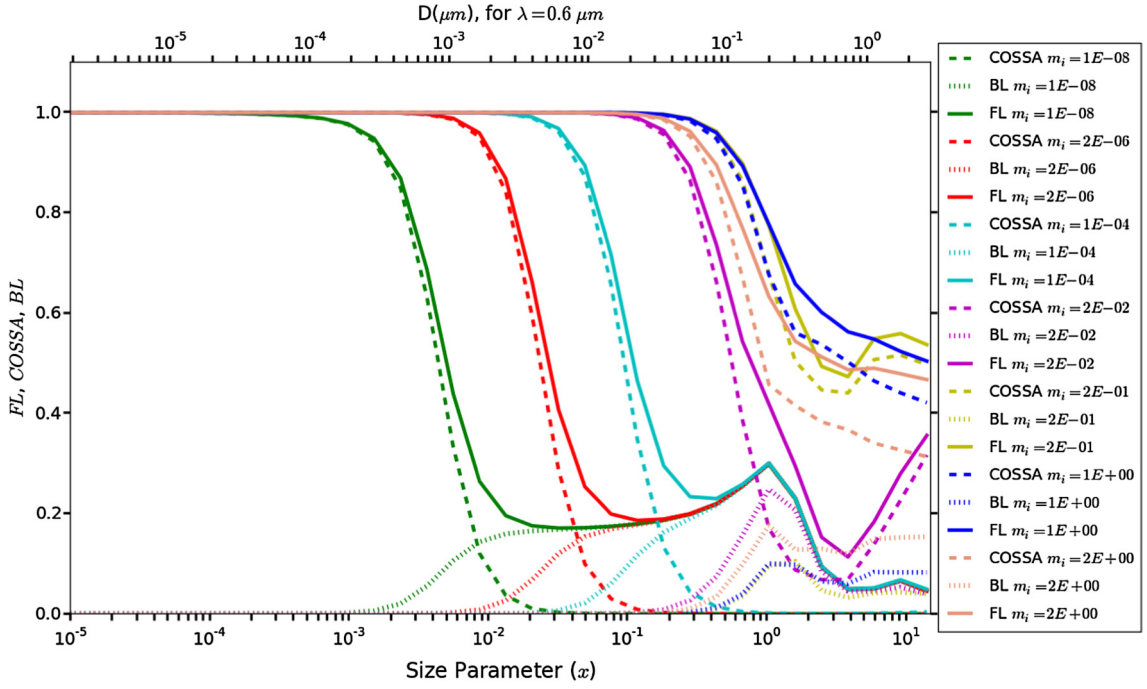

Fig. 6. *COSSA*, *BL*, and *FL* are displayed as function of size parameter for spherical particles on a substrate. The refractive index of the particles is $m = 1.5 + im_i$, while the substrate refractive index is $n = 1.5 + i0$. For reference, the upper horizontal axis shows the particle diameter for $\lambda = 0.6$ μm. Horizontally dashed lines represent *COSSA*; vertically dashed lines are *BL*, and the solid lines are *FL*. For each given m_i, the curves *COSSA*, *BL*, and *FL* are plotted in the same color.

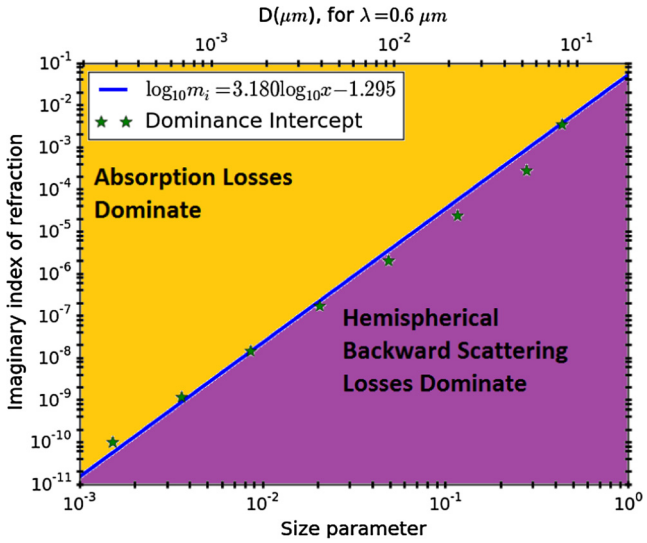

Fig. 7. The intercepts between BL and COSSA for the range $10^{-3} \lesssim x \lesssim 10^{0}$ are visible in Fig. 6. The imaginary part of the particle refractive index of these intercepts is plotted as a function of their size parameter in log-log space. For clarity, the upper horizontal axis shows the particle diameter for $\lambda = 0.6\ \mu m$ instead of the size parameter. The linear regression of these intercepts parameterizes this division and is shown as a solid line.

loss due absorption while BL indicates fractional power loss due to hemispheric backward scattering. The change in dominance between these processes is marked by the intercepts between *COSSA* and *BL* curves. It is noticeable that absorption dominates for small sizes and larger imaginary parts of the refractive index. The region of absorption dominance shifts toward larger size parameters for increasing m_i; notice the intercepts between $\sim 5 \times 10^{-2} \lesssim x \lesssim 2$ shifting right as m_i becomes larger. This indicates that as the diameter of small particles grows to $\gtrsim \frac{1}{3}$ of the wavelength (i.e., $x = 1$, or $D = \lambda/\pi$), for small imaginary parts of the refractive index (i.e. $m_i \lesssim 3 \times 10^{-2}$), the loss of power through hemispherical backward scattering become more significant than the loss caused by absorption. Interestingly, there is a limiting value of m_i above which there are no intercepts between *BL* and *COSSA* (i.e., absorption losses are always dominant). This limiting value was calculated numerically and is $m_i = 0.025 \pm 0.001$ using the DDA-substrate method; however, Mie theory, neglecting particle-substarte interaction, yields as slightly larger value of $m_i = 0.03 \pm 0.001$.

The intercepts between *BL* and *COSSA* in the region $10^{-2} \lesssim x \lesssim 10^{0}$ can be seen in Fig. 6. These intercepts and their values of imaginary index of refraction m_i and size parameter x divide the parameter space between dominance of either absorption or hemispherical backward scattering as the main mechanism of power loss for particles deposited on a PV cell. We have plotted these intercepts in Fig. 7, and have performed a linear regression in log-log space to describe this dividing line, yielding

$$\log_{10} m_i = 3.180 \log_{10} x - 1.295 \quad \text{for} \quad x < 1. \tag{35}$$

This regression subdivides the x vs m_i space domain into two regions. For any particle whose x and m_i values are in the upper left of the regression line, the main loss mechanism is absorption, while for x and m_i values in the lower right, the main loss mechanism is hemispherical backward scattering.

4.4. Particle scattering without and with substrate

Using DDA code is substantially more time consuming than using Mie code. Therefore, we explore the differences in results between these two approaches, investigating if the use of Mie code can be sufficient for scattering calculations involving spherical particles, in part of the parameter space. In Fig. 2, we notice that *FL* values calculated with Mie code are somewhat different from those calculated with DDA-substrate code. Hence, there exist a difference in *FL* depending on whether the substrate is included in our calculations or not.

Fig. 8 displays the difference in *FL*

$$\Delta FL = FL_{DDA-substrate} - FL_{MIE}, \tag{36}$$

between calculations of $FL_{DDA-substrate}$ using DDA-substrate and calculation of FL_{MIE} using Mie code.

Fig. 9 shows *COSSA* vs. x for different m_i values, calculated using Mie theory, which neglects the substrate, and DDA-substrate, which considers the substrate interaction. It is noticeable that there are no large differences between the curves by both methods.

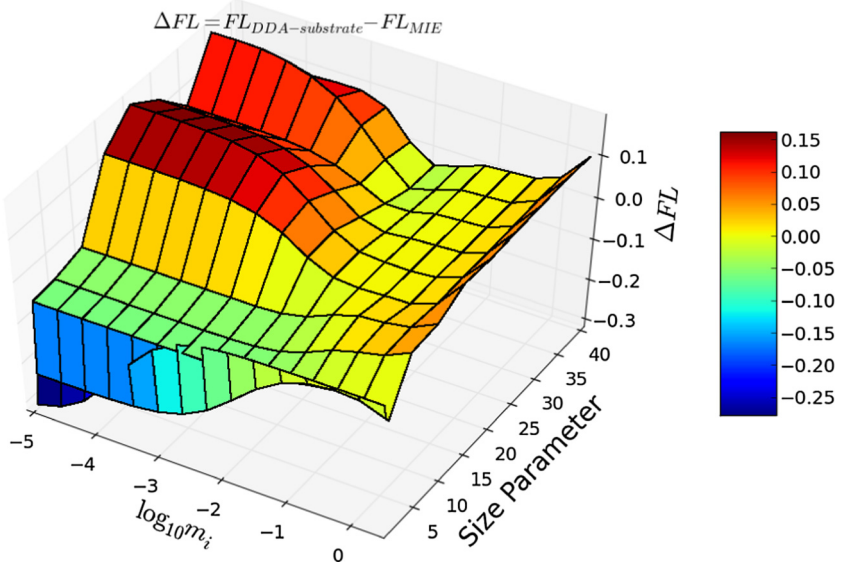

Fig. 8. We show the difference in power fraction lost *FL* between DDA-substrate and Mie theory calculations as a function of m_i and x. The calculations are for spherical aerosols of $m_r = 1.5 + im_i$, and the index of refraction of the substrate is $n = 1.5 + i0$.

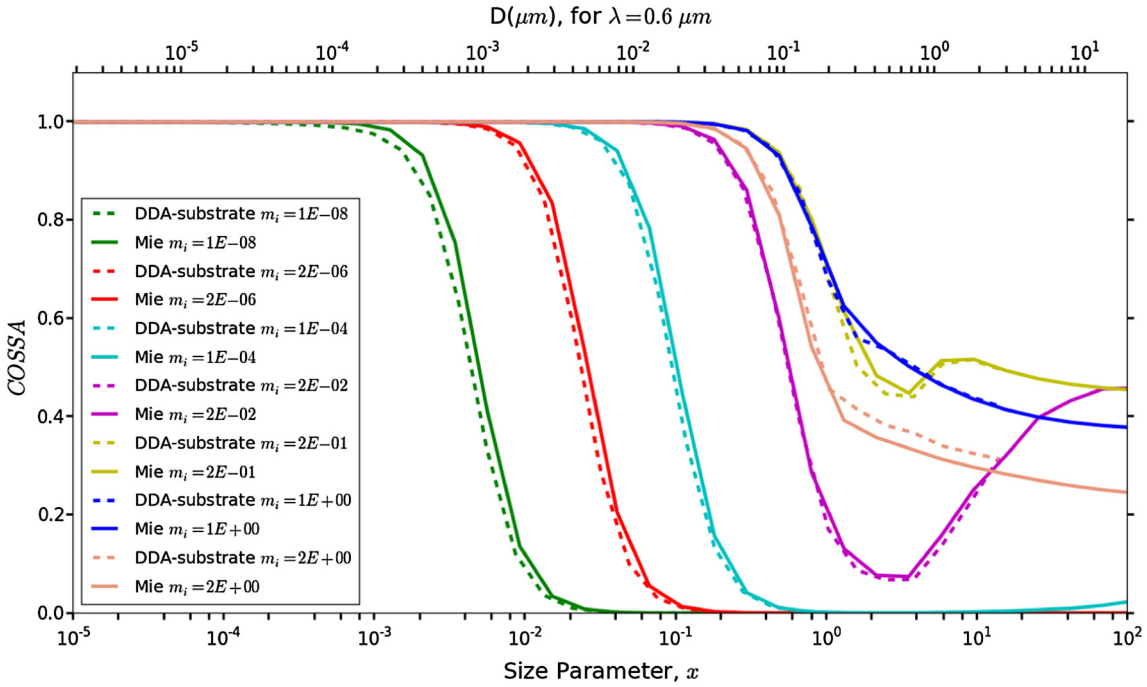

Fig. 9. Fractional losses due to absorption are quantified by *COSSA*. We display *COSSA* vs. x calculated using Mie theory (w/o substrate) and DDA-substrate (w/substrate). The calculation is for homogeneous spherical particles of $m_r = 1.5 + m_i$, where m_i is increased between $10^{-8} \leqslant m_i \leqslant 2$. The index of refraction of the substrate is $n = 1.5 = i0$. For clarity, each pair of *COSSA* curves Mie and DDA-substrate calculated at the same m_i is plotted in the same color. (For interpretation of the references to colour in this figure legend, the reader is referred to the web version of this article.)

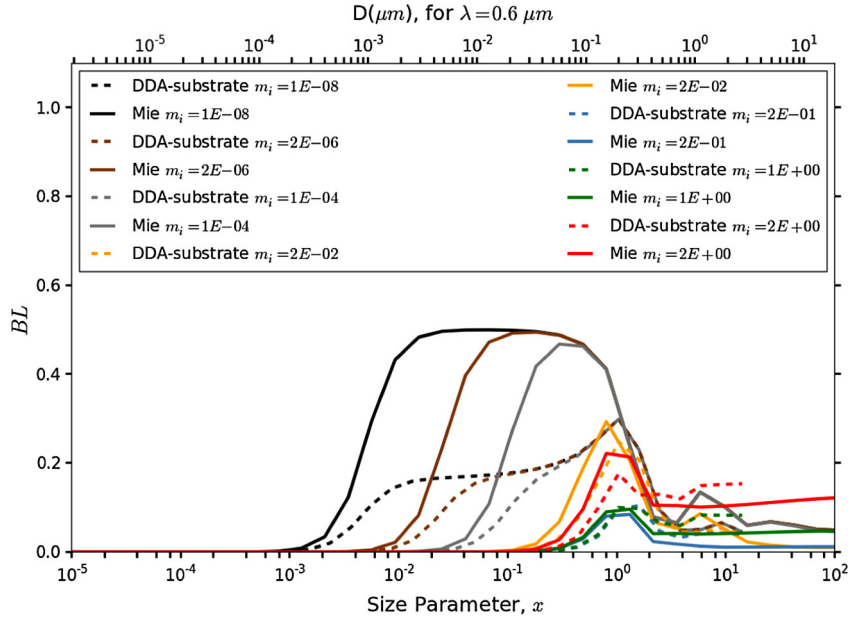

Fig. 10. *BL* vs. x curves calculated by Mie theory (w/o substrate) and by DDA-substrate (w/substrate) are shown. The calculation is for homogeneous spherical particles of $m_r = 1.5 + m_i$, where m_i is increased between $10^{-8} \leqslant m_i \leqslant 2$. The index of refraction of the substrate is $n = 1.5 + i0$. Each pair of *COSSA* curves Mie and DDA-substrate calculated at the same m_i is plotted in the same color. (For interpretation of the references to colour in this figure legend, the reader is referred to the web version of this article.)

This is expected since *COSSA* quantifies light extinction due to particle absorption, a mechanism which is largely independent of the substrate. However, in Fig. 10, we show that *BL* curves calculated without substrate (Mie theory) for small particles (i.e. $x \lesssim 1$) generally overestimate the *BL* values of DDA-substrate by nearly a factor of 2. This is because Mie theory does not account for frustrated internal reflection, a factor that decreases hemispherical backward scattering losses for small particles.

5. Conclusions

We studied power loss due to aerosol deposition on PV cells degrading their efficiency as function of particle size and imaginary part of the particle refractive index, that is as function of intrinsic optical characteristics of the deposited particles. This study contrasts with the large majority of publications that report optical losses of PV cells as function of exposure time to environmental

conditions (Mani and Pillai, 2010). Since these conditions can rapidly vary from day to day and geographical location, we concur with Al-Hasan (1998) who writes: "It is the amount of sand dust accumulated on the panels which should be correlated with light or solar radiation transmittance." Here, we followed this guidance and furthermore described a theory of particle optical losses that considers only those losses that reduce solar power production (i.e., absorption and scattering into the backward hemisphere) instead of extinction of the direct beam. This effectively modifies Beer-Lambert law to $P = P_0 e^{\tau FL}$, where FL is the fraction of the particle optical depth τ that results in reduced solar power production. We also described the hemispherical backward scattering and absorption efficiency $BSAE = Q_{ext} FL$, where all three parameters are intensive and not a function of mass per unit area on the PV cell. Second, we analyzed FL and $BSAE$ as functions of radius to skin depth fraction $m_i x$. We found that FL of small particles with $x \lesssim 1$ peaks at $FL \sim 1$ for $m_i x \approx 0.5$, while for large particles with $x \gtrsim 1$, FL peaks at $FL \sim 0.5$ for $m_i x \approx 2$. Similarly, $BSAE$ for small particles with $x \lesssim 1$ has a positive slope as function of $m_i x$ in log-log space, while for larger particles ($x \gtrsim 1$) $BSAE$ remains nearly constant as function of $m_i x$ up to $m_i x \sim 10^{-1}$, reaching a peak at $m_i x \approx 2$, Third, we described the mechanism causing optical losses with dominance of either hemispherical backward scattering or absorption in different parts of the parameter space. Fractional power losses caused by hemispherical backward scattering are described by BL while fractional power losses caused by absorption are described by co-albedo $COSSA$. For particles with size parameter $x \lesssim 1$ and $m_i \lesssim 0.025$, we find that the intercept between BL and $COSSA$ shifts towards larger x as m_i becomes larger. For particles with $m_i > 0.025$, absorption is always dominant, and there exists no intercept. Fourth, we described how optical interactions with the substrate modify particle optics compared to free space conditions, and how this affects FL. The $COSSA$ is mostly unaltered by the presence of a substrate since absorption is largely independent of the substrate interaction. However, BL is reduced by a factor of ~ 2 when the particles are small (i.e. $x \lesssim 1$) due to frustrated internal reflection. If the particle is $x \gtrsim 1$, BL is increased by ~ 0.1 due to increased hemispherical backward scattering caused by Fresnel reflection.

Overall, the behavior of power losses due to dust deposition quantified here can serve as an essential part of solar power forecasting if the thickness of the particle layer to be deposited can be estimated from atmospheric particle transport and deposition and if particle properties including size distribution and complex refractive index can be obtained from knowledge about the source region and entrainment and transport processes. However, it must be noted that this initial work assumes simplifications including normal incidence of the radiation, small particle loading, and homogeneous spherical particles (see Table 1). Further research is needed to extend our results beyond these simplifications, and we expect substantial new insights during this process.

Acknowledgments

This material is based upon work supported in part by the National Science Foundation's Solar Energy-Water-Environment Nexus in Nevada under Cooperative Support Agreement No. EPS-IIA-1301726. Patricio Piedra acknowledges Graduate Student Fellowships from the Nevada NASA Space Grant Consortium and from the Graduate Student Association of the University of Nevada, Reno. Hans Moosmuller acknowledges support from the Desert Research Institute Sabbatical Leave Program. It is a pleasure to acknowledge (1) the contributions of Vicken Etyemezian in encouraging and organizing this project, (2) many helpful discussions with Christopher Sorensen about the display of particle optical properties, and (3) Matthew Sgambati's support of our supercomputer use.

References

Al-Hasan, A.Y., 1998. A new correlation for direct beam solar radiation received by photovoltaic panel with sand dust accumulated on its surface. Sol. Energy 63 (5), 323–333.
Bohren, C.F., Huffman, D.R., 2008. Absorption and Scattering of Light by Small Particles. John Wiley & Sons.
Bond, T.C., Bergstrom, R.W., 2006. Light absorption by carbonaceous particles: an investigative review. Aerosol Sci. Technol. 40 (1), 27–67.
Chamaillard, K., Jennings, S., Kleefeld, C., Ceburnis, D., Yoon, Y., 2003. Light backscattering and scattering by nonspherical sea-salt aerosols. J. Quant. Spectrosc. Radiat. Transfer 79, 577–597.
Darwish, Z.A., Kazem, H.A., Sopian, K., Al-Goul, M., Alawadhi, H., 2015. Effect of dust pollutant type on photovoltaic performance. Renew. Sustain. Energy Rev. 41, 735–744.
Draine, B.T., Flatau, P.J., 1994. Discrete-dipole approximation for scattering calculations. JOSA A 11 (4), 1491–1499.
Engelbrecht, J.P., Moosmüller, H., Pincock, S., Jayanty, R.M., Lersch, T., Casuccio, G., 2016. Technical note: Mineralogical, chemical, morphological, and optical interrelationships of mineral dust re-suspensions. http://www.atmos-chem-phys.net/16/10809/2016/.
Formenti, P., Schütz, L., Balkanski, Y., Desboeufs, K., Ebert, M., Kandler, K., Petzold, A., Scheuvens, D., Weinbruch, S., Zhang, D., 2011. Recent progress in understanding physical and chemical properties of african and asian mineral dust. Atmos. Chem. Phys. 11 (16), 8231–8256.
Levoni, C., Cervino, M., Guzzi, R., Torricella, F., 1997. Atmospheric aerosol optical properties: a database of radiative characteristics for different components and classes. Appl. Opt. 36 (30), 8031–8041.
Li, Y., Vu, N., Kim, A.S., 2009. 3-d monte carlo simulation of particle deposition on a permeable surface. Desalination 249 (1), 416–422.
Mackowski, D.W., 2008. Exact solution for the scattering and absorption properties of sphere clusters on a plane surface. J. Quant. Spectrosc. Radiat. Transfer 109 (5), 770–788.
Maghami, M.R., Hizam, H., Gomes, C., Radzi, M.A., Rezadad, M.I., Hajighorbani, S., 2016. Power loss due to soiling on solar panel: a review. Renew. Sustain. Energy Rev. 59, 1307–1316.
Maltsev, V.P., Hoekstra, A.G., Yurkin, M.A., 2011. Optics of white blood cells: optical models, simulations, and experiments. Exp. Tech. 4 (3).
Mani, M., Pillai, R., 2010. Impact of dust on solar photovoltaic (pv) performance: research status, challenges and recommendations. Renew. Sustain. Energy Rev. 14 (9), 3124–3131.
Mie, G., 1908. Pioneering mathematical description of scattering by spheres. Ann. Phys 25, 337.
Moosmüller, H., Chakrabarty, R., Arnott, W., 2009. Aerosol light absorption and its measurement: a review. J. Quant. Spectrosc. Radiat. Transfer 110 (11), 844–878.
Moosmüller, H., Engelbrecht, J.P., Skiba, M., Frey, G., Chakrabarty, R.K., Arnott, W.P., 2012. Single scattering albedo of fine mineral dust aerosols controlled by iron concentration. J. Geophys. Res.: Atmos. 117 (D11).
Pelland, S., Remund, J., Kleissl, J., Oozeki, T., De Brabandere, K., 2013. Photovoltaic and solar forecasting: state of the art. IEA PVPS, Task, 14.
Polyansky, M.N., 2016. Refractive Index Database. <http://refractiveindex.info>.
Reddington, C., McMeeking, G., Mann, G., Coe, H., Frontoso, M., Liu, D., Flynn, M., Spracklen, D., Carslaw, K., 2013. The mass and number size distributions of black carbon aerosol over europe. Atmos. Chem. Phys. 13 (9), 4917–4939.
Ryder, C., Highwood, E., Rosenberg, P., Trembath, J., Brooke, J., Bart, M., Dean, A., Crosier, J., Dorsey, J., Brindley, H., 2013. Optical properties of saharan dust aerosol and contribution from the coarse mode as measured during the fennec 2011 aircraft campaign. Atmos. Chem. Phys. 13 (1), 303–325.
Schmehl, R., 1994. The coupled-dipole method for light scattering from particles on plane surfaces. Arizona State University, Dept. of Mechanical and Aerospace Engineering.
Seinfeld, J.H., Pandis, S.N., 2012. Atmospheric Chemistry and Physics: from Air Pollution to Climate Change. John Wiley & Sons.
Sulaiman, S.A., Singh, A.K., Mokhtar, M.M.M., Bou-Rabee, M.A., 2014. Influence of dirt accumulation on performance of pv panels. Energy Procedia 50, 50–56.
Tan, C.L.C., Gao, S., Wee, B.S., Asa-Awuku, A., Thio, B.J.R., 2014. Adhesion of dust particles to common indoor surfaces in an air-conditioned environment. Aerosol Sci. Technol. 48 (5), 541–551.
van de Hulst, H., 1981. Light Scattering by Small Particles. Dover.
Videen, G., 1995. Light scattering from a particle on or near a perfectly conducting surface. Opt. Commun. 115 (1–2), 1–7.
Wang, G., Chakrabarti, A., Sorensen, C.M., 2015. Effect of the imaginary part of the refractive index on light scattering by spheres. JOSA A 32 (7), 1231–1235.
Wriedt, T., Doicu, A., 1998. Light scattering from a particle on or near a surface. Opt. Commun. 152 (4), 376–384.
Yurkin, M.A., Hoekstra, A.G., 2011. The discrete-dipole-approximation code adda: capabilities and known limitations. J. Quant. Spectrosc. Radiat. Transfer 112 (13), 2234–2247.